An Improved Spatiotemporal Savitzky–Golay (iSTSG) Method to Improve the Quality of Vegetation Index Time-Series Data on the Google Earth Engine

Weiyi Wang, Ruyin Cao, Licong Liu, Ji Zhou, *Senior Member, IEEE*, Miaogen Shen, Xiaolin Zhu, *Senior Member, IEEE*, and Jin Chen

***Abstract*— MODerate-resolution Imaging Spectroradiometer (MODIS) vegetation index (VI) time-series data are among the most widely utilized remote sensing datasets. To improve the quality of MODIS VI time-series data, most prior methods have focused on correcting negatively biased VI noise by approaching the upper envelope of the VI time series. Such treatment, however, may cause overcorrections on some true local low VI values, resulting in inaccurate simulations of vegetation phenological characteristics. In addition, another challenge in reconstructing MODIS VI time series is to fill temporally continuous gaps. The earlier spatiotemporal Savitzky–Golay (STSG) method tackled this problem by utilizing multiyear VI data, but its performance heavily relies on the consistency of data across different years. In this study, we proposed an improved STSG (iSTSG) method. The new method accounts for the autocorrelation within the VI time series and fills missing values in the VI time series by leveraging spatiotemporal VI data from the current year alone. Furthermore, iSTSG incorporates an indicator to quantify potential overcorrections in the VI time series, aiming to more accurately simulate phenological characteristics. The experiments to reconstruct MODIS normalized difference VI (NDVI) time-series product (MOD13A2) at four typical sites (a million square kilometers for each site) suggest two clear advantages in iSTSG over the iterative SG (called Chen-SG) and STSG methods. First, iSTSG more accurately reconstructs the annual NDVI time series, exhibiting the smallest mean absolute differences (MADs) between the smoothed and the simulated reference NDVI time series (0.012, 0.018, and 0.020 for iSTSG, STSG, and Chen-SG, respectively). Second, iSTSG more effectively simulates phenological characteristics in the NDVI time series, including the onset dates for vegetation greenup and dormancy, as well as the crop harvest period. The advantages of iSTSG were also demonstrated when applied to the successor of MODIS, Visible Infrared Imaging Radiometer Suite (VIIRS) VI time-series product (VNP13A1). iSTSG can be implemented on the Google Earth Engine (GEE), offering significant benefits for various applications, particularly in crop mapping and vegetation/crop phenology studies.**

***Index Terms*— Crop phenology, normalized difference vegetation index (NDVI) reconstruction, time-series smooth, vegetation phenology, Visible Infrared Imaging Radiometer Suite (VIIRS) NDVI.**

I. Introduction

THE time series of normalized difference vegetation index (NDVI) and enhanced vegetation index (EVI) data provided by the MODerate-resolution Imaging Spectroradiometer (MODIS) have been extensively utilized to study various land surface parameters, including leaf area index [1], vegetation phenology [2], and land covers [3]. While high-quality MODIS NDVI/EVI time-series data are crucial for these applications, the vegetation index (VI) time-series data are easily contaminated by adverse atmospheric conditions (e.g., cloud cover). The maximum-value composition technique [4] has been employed to generate the MODIS VI time-series data, but residual noise in these products still requires elimination.

Numerous methods have been developed to eliminate residual noise in the MODIS VI time-series products [5], [6]. Early methods can be categorized as temporal-based, utilizing various temporal filters to smooth the original VI time series or employing different mathematical functions to model annual trajectories of the VI time series. Temporal filters used to smooth the VI time series include the iterative Savitzky–Golay (SG) filter [7], harmonic analysis of time series [8], the mean-value iteration filter [9], the changing-weight filter [10], and the Whittaker filter [11]. Mathematical functions employed by previous methods include the double logistic function [12], the asymmetric Gaussian function [13], and the Fourier and wavelet transforms [14], [15]. Some studies compared the performance of different temporal-based methods, yet no clear consensus has emerged regarding the best approach [16], [17]. Clearly, it is challenging to use the temporal-based methods to reconstruct long-term missing

Received 24 August 2024; revised 4 December 2024; accepted 7 January 2025. Date of publication 16 January 2025; date of current version 29 January 2025. This work was supported in part by the National Natural Science Foundation of China under Grant U23A2018 and Grant 42271379 and in part by Sichuan Science and Technology Program under Grant 2025YFHZ0228. *(Corresponding author: Ruyin Cao.)*

Weiyi Wang, Ruyin Cao, and Ji Zhou are with the School of Resources and Environment, University of Electronic Science and Technology of China, Chengdu 611731, China (e-mail: cao.ruyin@uestc.edu.cn).

Licong Liu, Miaogen Shen, and Jin Chen are with the State Key Laboratory of Earth Surface Processes and Resource Ecology, Faculty of Geographical Science, Institute of Remote Sensing Science and Engineering, Beijing Normal University, Beijing 100875, China.

Xiaolin Zhu is with the Department of Land Surveying and Geo-Informatics, The Hong Kong Polytechnic University, Hong Kong, China.

This article has supplementary downloadable material available at https://doi.org/10.1109/TGRS.2025.3528988, provided by the authors.

Digital Object Identifier 10.1109/TGRS.2025.3528988

values in the VI time series. In recent years, more sophisticated methods integrating spatiotemporal information have been proposed to reconstruct the MODIS VI time-series data. These methods account for both spatial correlations among pixels in neighboring windows and temporal correlations of VI data across multiple years, achieving markedly better performance in reconstructing VI time series with continuous data gaps. The typical spatiotemporal-based methods include the spatiotemporal SG (STSG) method [18], the spatiotemporal tensor completion method [19], and the spatiotemporal prefill method with harmonic analysis of time series [20].

The SG filter, a simplified least-square-fit convolution [21], has undergone continuous modifications over the past two decades to reconstruct VI time-series data. We have identified two significant advancements within the family of SG-based methods. The first is the iterative SG method proposed by Chen et al. [7] (hereafter referred to as the Chen-SG method). In this method, data noise in the VI time-series was assumed to be negatively biased and corrected through an iterative procedure to approach the upper envelope of the original VI time-series data. The Chen-SG method has been employed in thousands of geography and ecology studies to preprocess VI time-series data, accumulating over 1800 citations on the Web of Science as of November 2023. Actually, the principle of approaching the upper envelope has indeed been widely adopted in subsequent methods utilizing other smoothing filters [6], [22]. The second advancement is the integration of spatiotemporal information into the SG filtering process, resulting in the STSG method [18]. This method assumes that clouds are spatially discontinuous and employs neighboring pixels to assist in noise reduction for the target pixel. Compared with the Chen-SG method, STSG more effectively reconstructs temporally continuous missing values and partially alleviates the overcorrections of the true low VI values caused by crop harvests. The computational efficiency of STSG was further enhanced by implementing a parallel procedure on graphics processing units [23].

Despite the progress in methods to reconstruct MODIS VI time series, we have identified two important issues that previous SG-based methods have not adequately addressed. First, although integrating spatiotemporal information with the SG filter is essential, the STSG method requires multiyear VI data to establish the relationship between the VI time series of the target pixel and its neighboring pixels. When using multiyear VI time-series data, the performance depends on the consistency of the data across different years. Several factors affect data consistency, including significant variations in vegetation phenology across years, abrupt land surface changes in the current year, and inaccuracies in cloud masking in some years. In addition, the collection and processing of multiyear VI time series is labor-intensive, limiting the application of STSG in large-scale areas [23]. Our tests of the computation efficiency of STSG show that processing VI time series with STSG takes more than 20 times longer than the Chen-SG method (see experiments in this study). Therefore, it is preferable to use the VI data from the current year only while simultaneously addressing the shortcomings of Chen-SG method, such as poor performance for long-term data gaps and overcorrections of true low VI values.

The second issue is enhancing the simulation of vegetation phenological characteristics in the VI time-series data. In striving to approach the upper envelope of VI time-series data, Chen-SG and STSG methods iteratively fit the VI time series and preserve higher VI values in each iteration; consequently, local low VI values may not be accurately simulated, leading to systematic errors in vegetation phenology estimates [24]. An illustrative example highlights this issue. For an ideal double logistic VI curve, the greenup onset date (GOD) and dormancy onset date (DOD) are defined at 105 days of year (DOY) and 265 DOY, respectively, following the definitions by Liu et al. [22] [Fig. 1(a)]. Applying the Chen-SG method to this VI curve, we observed that the segments around GOD and DOD in the smoothed VI time series were significantly elevated compared to that in the original VI time series. Consequently, GOD and DOD are identified at 100 DOY (five days earlier) and 271 DOY (six days later) in the smoothed VI time series, respectively. Fig. 1(b) simulates a crop harvest period within the VI time series. However, these local low VI values were incorrectly elevated by both the Chen-SG method [Fig. 1(b)] and the STSG method (see Cao et al. [18, Fig. 3(D)], potentially hindering applications such as cropping intensity and crop type mapping. Thus, preserving phenological characteristics in reconstructed VI time-series data has been overlooked in previous methods and requires particular attention.

To address these issues, we proposed an improved spatiotemporal SG method (referred to as iSTSG) to reconstruct high-quality VI time-series data from MODIS and its successor Visible Infrared Imaging Radiometer Suite (VIIRS). This new method addressed the two unsolved issues explained above and outperformed previous SG-based methods in comprehensive testing experiments. In addition, iSTSG can be implemented on the Google Earth Engine (GEE) platform, significantly enhancing the accessibility and application of the new method in the relevant geography and ecology studies.

II. Materials and Methods

A. MODIS VI Time-Series Data

We evaluated the performance of iSTSG using the MODIS VI time-series product (MOD13A2 V061; Didan, 2021) [25]. The MOD13A2 product offers two VIs (NDVI and EVI) with a spatial resolution of 1 km and a temporal resolution of 16 days. Therefore, there are 23 VI data points in the annual VI time series. Besides the VI data, the product includes a data quality layer that indicates the quality of the VI value for each pixel on each composition date. VI values of good quality (i.e., cloud- and snow-free) have a pixel reliability index (RI) of 0, while those with some uncertainty have an RI of 1. Contaminated VI values are labeled as -1 (no data), 2 (snow and ice), or 3 (cloud). Due to page limitation, we reported the experiments using the MODIS NDVI time-series data in Section IV and discussed the applicability of the new method for the MODIS EVI time-series data as well as the VIIRS VI data in Section V.

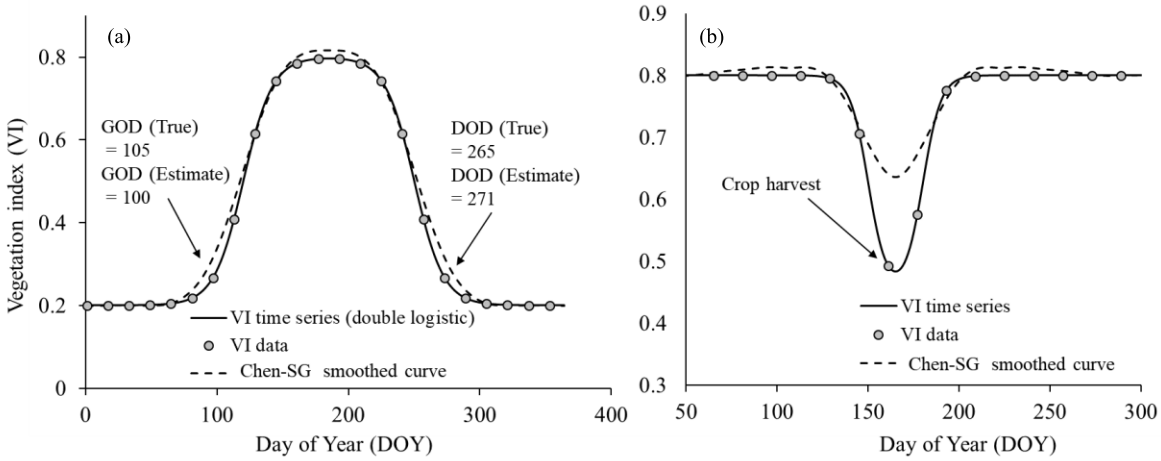

Fig. 1. (a) Example showing the VI deviations in the local segment around the GOD and DOD. According to the rates of curvature changes [2], the GOD estimated from Chen-SG smoothed curve is five days earlier than the true value, and the estimated DOD is six days later than the true value. (b) Example showing overcorrections on the local low VI values during the crop harvest period by the Chen-SG method.

B. iSTSG Method

The iSTSG method utilizes the same input data as the Chen-SG method, specifically the VI time-series data for the current year only. The objectives of the iSTSG method are to more effectively address continuous data gaps in the VI time series and simulate vegetation phenological characteristics. The new method accomplishes the objectives in two main steps, which are illustrated in detail in the following.

Step 1 (Generating Initial VI Estimates With Autocorrelation of the VI Time Series): To smooth the VI time-series data using the SG filter, the first step in Chen-SG method Sis to fill those missing VI values (i.e., RI values of -1, 2, and 3) through linear interpolations [7]. This operation may be effective for the local VI segments in the time series with nearly linear changes, but it poses challenges for temporally continuous missing VI values or the VI segments with obvious nonlinear characteristics. In addition, some VI values in the VI time series are labeled as uncertain values (i.e., RI value of 1), indicating potential contamination in these VI values. These uncertain VI values need to be processed before smoothing the VI time series. Therefore, in the first step, the iSTSG method generates initial VI estimates for the missing and uncertain VI values based on autocorrelation of the VI time series.

For a missing or uncertain VI value at the date Ti in the VI time series of a target pixel p_0 (referred to as $\mathrm{VI}_{p_0}^{Ti}$), its initial value ($\mathrm{VI}_{p_0}^{Ti}$(initial)) can be estimated from the VI values within a temporal window centered at Ti (Fig. 2), given by

$$\mathrm{VI}_{p_0}^{Ti}(\text{initial}) = \text{median}(a_{Tj} \times \mathrm{VI}_{p_0}^{Tj} + b_{Tj}) \quad Tj \in [Ti - tw, Ti + tw] \tag{1}$$

where $\mathrm{VI}_{p_0}^{Tj}$ represents the VI values at the date Tj; a_{Tj} and b_{Tj} are the slope and intercept in the linear regression, respectively; and tw represents the size of the half temporal window. Due to the scarcity of good quality VI values in some cloudy areas, (1) uses the VI values within the temporal window labeled as good or uncertain (i.e., RI values of 0 or 1 for $\mathrm{VI}_{p_0}^{Tj}$). In addition, $\mathrm{VI}_{p_0}^{Tj}$ values smaller than a specified threshold (e.g., NDVI < 0.15) are excluded to prevent the influence of nonvegetation on the regression. Utilizing both good and uncertainty values in (1) is acceptable because individual contaminated $\mathrm{VI}_{p_0}^{Tj}$ less affect the initial estimate $\mathrm{VI}_{p_0}^{Ti}$(initial) by selecting the median value among a number of estimates [i.e., the median function in (1)]. To estimate a_{Tj} and b_{Tj} in (1), the spatial neighboring pixels similar to the target pixel were employed, which are expressed as

$$(a_{Tj}, b_{Tj}) = \underset{(a_{Tj}, b_{Tj})}{\arg\min} \frac{1}{n} \sum_{k=1}^{n} \left[\left(a_{Tj} \times \mathrm{VI}_{p_k}^{Tj} + b_{Tj} \right) - \mathrm{VI}_{p_k}^{Ti} \right]^2 \tag{2}$$

where $\mathrm{VI}_{p_k}^{Ti}$ and $\mathrm{VI}_{p_k}^{Tj}$ represent the good or uncertain VI values at the dates Ti and Tj in the VI time series of a spatial neighboring pixel p_k, respectively, and n denotes the number of similar pixels within a spatial window centered at the target pixel p_0. Here, we calculated the correlation coefficients between the annual VI time series of neighboring pixels and that of the target pixel p_0 using only good and uncertainty VI values, defining similar pixels as the ones with correlation coefficients above 0.85. The size of half spatial window, denoted as sw, is a crucial parameter and needs to be determined. By combining (1) and (2), it can estimate the initial VI values for the missing and uncertain VI values of the target pixel p_0. Some initial VI values in the VI time series may not be generated due to spatially and temporally continuous missing values, we adopted the same operations as the Chen-SG method to fill these values by linear interpolation. The two key parameters tw and sw were determined through a parameter sensitive experiment (see experimental results in Section IV-A).

Step 2 (Preserving Phenological Characteristics in the Iterative SG Filter): We first corrected the VI values in the original VI time series by using the initial VI estimates acquired in the first step. Specifically, the missing VI values in the original VI time series were directly replaced by the corresponding initial VI estimates. For the uncertain VI values in the original VI time series, we compared them with the corresponding initial VI estimates and selected the larger values, considering the

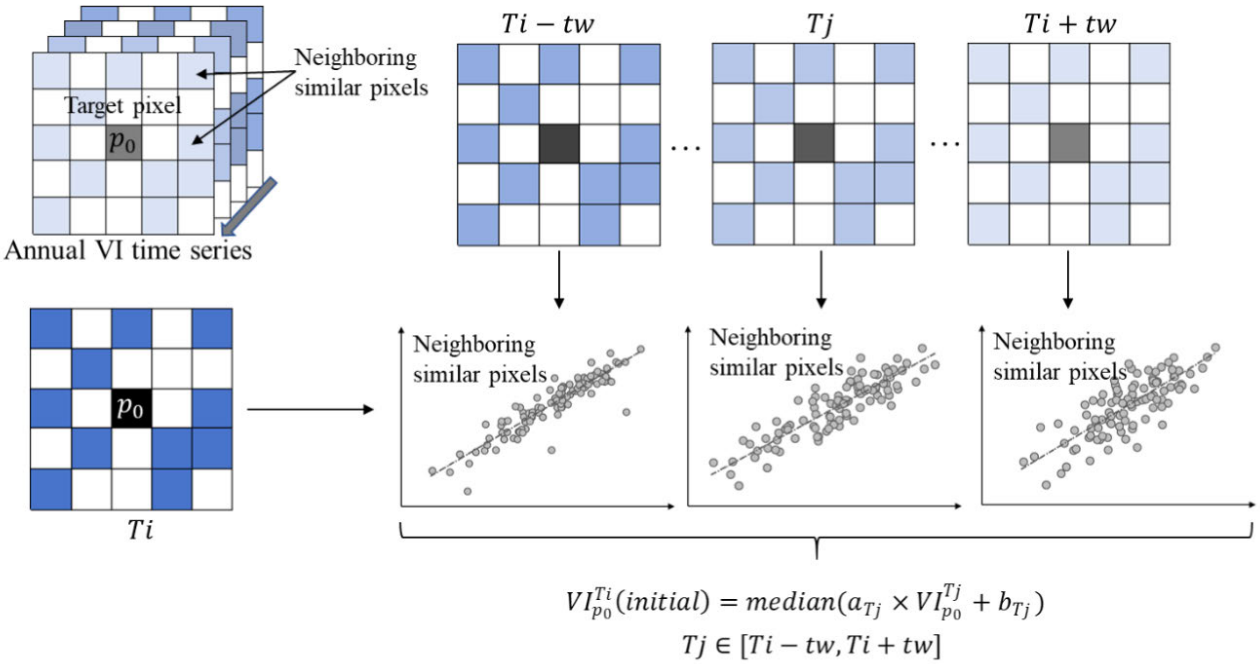

Fig. 2. Sketch to show the estimation of VI value at the date Ti in the VI time series of a target pixel p_0 ($\mathrm{VI}_{p_0}^{Ti}(\mathrm{initial})$). tw is the size of the half temporal window.

fact that contaminated VI (NDVI and EVI) values are usually negatively biased. The VI time series after the correction was referred to as the corrected VI time series [VI(corrected)] in the following statements.

It remains necessary to smooth VI(corrected) to remove possible residual noise while preserving vegetation phenological characteristics in the smoothed VI time series. Therefore, we first applied the SG filter to VI(corrected), referred to as $\mathrm{SG}[\mathrm{VI}(\mathrm{corrected})]_1$, and then determined the VI value in the filtered VI time series as the maximum value between VI(corrected) and $\mathrm{SG}[\mathrm{VI}(\mathrm{corrected})]_1$. There are two parameters in the SG filter, i.e., the order of polynomial and the size of the smoothing window. We followed [7] to use a 90-day smoothing window, within which there were approximately seven NDVI points with 16-day intervals. Considering the number of NDVI points in each smoothing window, the order of the polynomial was set to 4. Using the SG filter once, obvious individual VI noise points in VI(corrected) can be processed, such as a sudden drop VI point. To approach the upper envelope of VI(corrected), we repeated this process, which is expressed as

$$\mathrm{VI}_{p_0}^{Ti}(\mathrm{filtered})_k = \max\left(\mathrm{VI}_{p_0}^{Ti}(\mathrm{corrected}), \mathrm{SG}[\mathrm{VI}(\mathrm{corrected})]_k\right) \tag{3}$$

where $\mathrm{VI}_{p_0}^{Ti}(\mathrm{filtered})_k$ represents the filtered VI value at time Ti for the target pixel p_0 in kth repetitions. According to (3), the VI time series for the target pixel p_0 can be generated

$$\mathrm{VI}_{p_0}(\mathrm{filtered})_k = [\mathrm{VI}_{p_0}^{1}(\mathrm{filtered})_k, \mathrm{VI}_{p_0}^{2}(\mathrm{filtered})_k, \ldots, \mathrm{VI}_{p_0}^{23}(\mathrm{filtered})_k].$$

This process was repeated three times (i.e., $k = 3$) because the upper envelope is typically approached after applying SG filters three times, as observed in our results and previous studies (see [7, Fig. 3]). As previously mentioned, vegetation phenological characteristics occurring in the VI segments with local low values may not be simulated well in $\mathrm{VI}_{p_0}(\mathrm{filtered})_3$. We proposed an indicator to identify these positions in $\mathrm{VI}_{p_0}(\mathrm{filtered})_3$. In specific, for the target pixel p_0 at time Ti ($Ti = 1, 2, \ldots, 23$), this indicator quantifies the relationship between the VI value at Ti ($\mathrm{VI}_{p_0}^{Ti}(\mathrm{corrected})$) and the VI values in the temporal window at both sides of centered at Ti ($\mathrm{VI}_{p_0}^{Ti\_tw}(\mathrm{corrected})$), given as shown at the bottom of the page, where

$$\mathrm{meanV} = \mathrm{mean}\left(\mathrm{VI}_{p_0}^{Ti\_tw}(\mathrm{corrected})/\{\mathrm{VI}_{p_0}^{Ti}(\mathrm{corrected})\}\right). \tag{4}$$

The item meanV indicates the mean of VI values in the temporal window, excluding the center time Ti (i.e., formulated as "mean($\mathrm{VI}_{p_0}^{Ti\_tw}(\mathrm{corrected})/\{\mathrm{VI}_{p_0}^{Ti}(\mathrm{corrected})\}$)"). The denominator in (4) normalizes $\mathrm{Indic}_{p_0}^{Ti}$ to be between 0 and 1. $\mathrm{Indic}_{p_0}^{Ti}$ has a larger value when $\mathrm{VI}_{p_0}^{Ti}(\mathrm{corrected})$ is closer to the minimum or maximum VI values in the temporal window. The final estimate of $\mathrm{VI}_{p_0}^{Ti}$ was generated

$$\mathrm{Indic}_{p_0}^{Ti} = \frac{\left|\mathrm{VI}_{p_0}^{Ti}(\mathrm{corrected}) - \mathrm{meanV}\right|}{\max\left(\max\left(\mathrm{VI}_{p_0}^{Ti\_tw}(\mathrm{corrected})\right) - \mathrm{meanV}, \mathrm{meanV} - \min\left(\mathrm{VI}_{p_0}^{Ti\_tw}(\mathrm{corrected})\right)\right)}$$

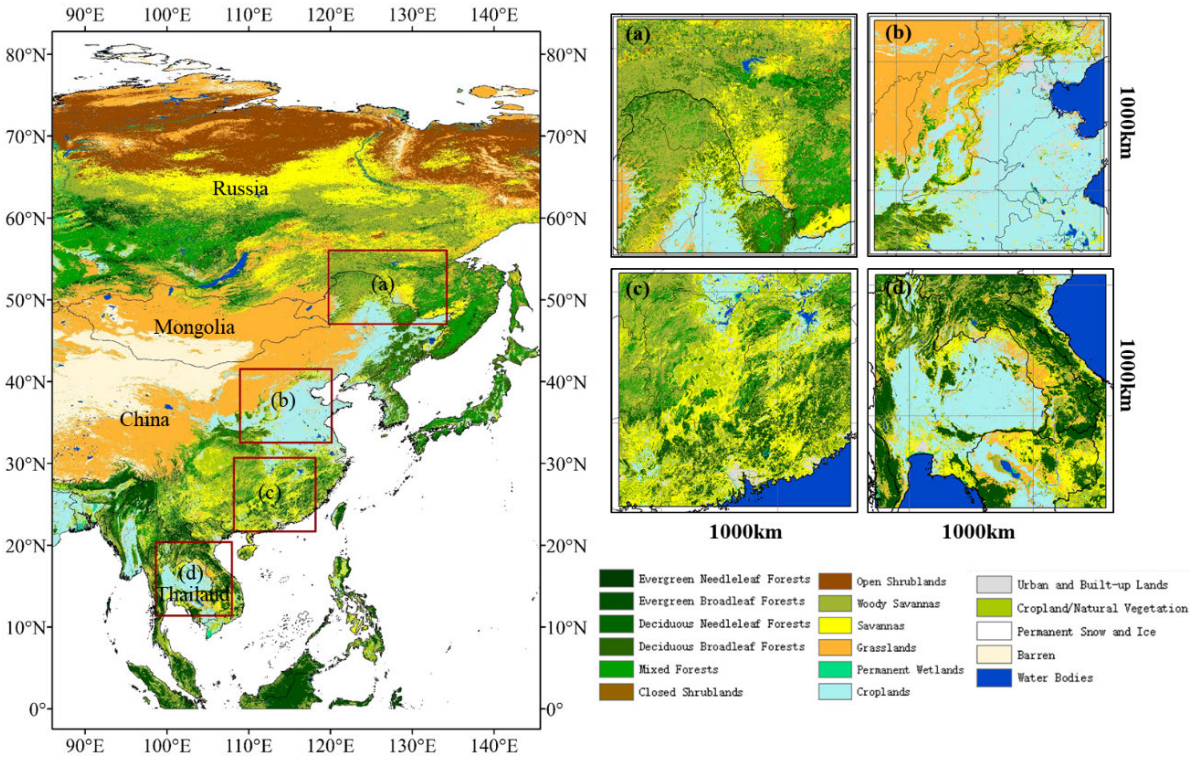

Fig. 3. Locations and land cover types of the four testing sites. (a) Northeastern Asia, (b) North China Plain, (c) Southeastern China, and (d) Southeastern Asia. Each testing site has an area of 1000 × 1000 km. The land cover data are provided by the MODIS land cover product MCD12Q1 [3].

by combining $\mathrm{VI}_{p_0}^{Ti}(\mathrm{filtered})_1$ and $\mathrm{VI}_{p_0}^{Ti}(\mathrm{filtered})_3$ as

$$\mathrm{VI}_{p_0}^{Ti}(\mathrm{filtered})_{\mathrm{final}} = \mathrm{Indic}_{p_0}^{Ti} \times \mathrm{VI}_{p_0}^{Ti}(\mathrm{filtered})_1 + \left(1 - \mathrm{Indic}_{p_0}^{Ti}\right) \times \mathrm{VI}_{p_0}^{Ti}(\mathrm{filtered})_3. \quad (5)$$

Therefore, the iSTSG method avoids overcorrection by considering the shapes of NDVI time series in local segments. In the experiments, we tested the performance of iSTSG in reducing noise and preserving phenological characteristics in the VI time series

C. Testing Sites

We tested the performance of iSTSG at four typical sites with an area of 1000 × 1000 km at each site (Fig. 3). The first site is located across northeastern China and eastern Russia (referred to as northeastern Asia), predominantly covered by deciduous forests and grasslands. The second site is the North China Plain, which is mainly covered by double-season croplands and grasslands. Winter wheat is harvested during May and June, followed by corn planting, resulting in a VI time series with two peaks within a year. The third site is in southeastern China, characterized by a mixture of evergreen and deciduous forests. The fourth site is in southeastern Asia, covering most areas of Thailand, where rice is the main crop. Approximately 75% of the rice is single-cropped during the rainy season (May–October), while the remaining 25% is double-cropped, planted in both rainy and dry seasons.

The four sites were selected because they can adequately test the performance of different methods. Southeastern China [Fig. 3(c)] and southeastern Asia [Fig. 3(d)] present challenging scenarios due to their cloudy and rainy conditions and subtropical and tropical monsoon climates, leading to temporally continuous missing values in the VI time series. The double-season crops in North China Plain [Fig. 3(b)] have relatively complex annual VI curves, most previous NDVI smoothing filters cannot reconstruct well [18]. In the experiments, we reconstructed the MODIS NDVI time series in 2020 at each testing site.

III. Experiments

A. Benchmark Methods for Comparisons

As a new member in the family of SG-based methods, iSTSG was compared with the Chen-SG method [7] and the STSG method [18]. The Chen-SG method has been widely used in relevant applications during the past two decades. Both the iSTSG method and the Chen-SG method can be applied to the one-year VI time series. Different from the two methods, STSG requires multiyear VI time series as input data. Specifically, STSG establishes the relationship between a target pixel and its neighboring similar pixels for each date, utilizing historical VI data from that date. This relationship is then used to generate initial VI estimates for each date. Finally, a weighted SG filter is applied to smooth the VI time series, with weights defined based on the uncertainty of each NDVI observation, accounting for potential cloud contamination (for algorithm details, please refer to Cao et al. [18]). We implemented the Chen-SG and STSG methods using the publicly available source codes provided by their authors. To compare computational efficiency, all three methods were programmed on the GEE with the same programming language (see discussion in Section V-A).

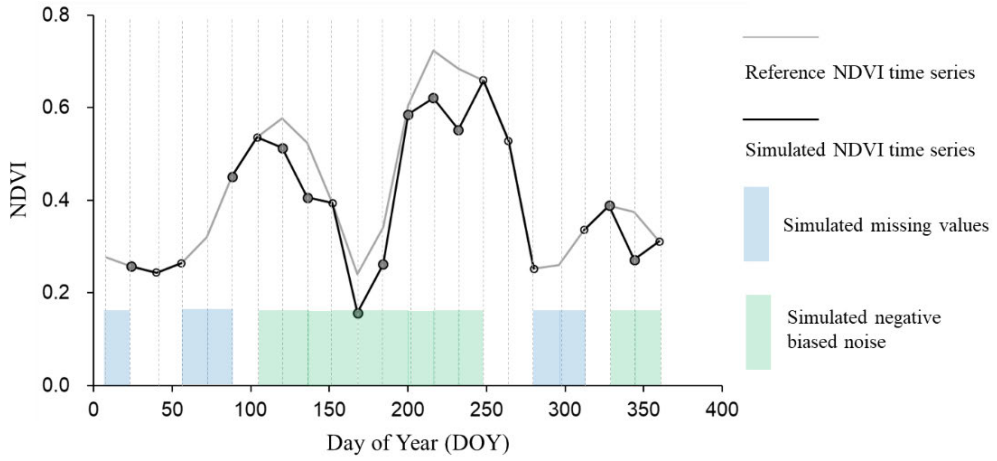

Fig. 4. Example showing the simulated NDVI time series. The reference and simulated NDVI time series are indicated by the gray and black lines, respectively.

B. Experiment Design

We designed four experiments. In the first experiment, we determined key parameter values in iSTSG through parameter sensitivity analyses, in which different parameter combinations were tested. In the second experiment, we applied the three SG-based methods to the real NDVI time-series data and conducted qualitative assessments by visually inspecting the NDVI images and NDVI time-series data smoothed by different methods. In the third experiment, we followed previous studies [17] to generate simulated NDVI time-series data for quantitative assessments (see details in Section III-C). The mean absolute differences (MADs) between the smoothed NDVI and reference NDVI time-series data were used to quantify overall fidelity. In addition, given that the iSTSG method consists of two steps, an ablation experiment was designed to test the effectiveness of each step. In the fourth experiment, we focused on evaluating the ability to simulate vegetation phenological characteristics in local segments of the NDVI time-series data (see details in Section III-D).

C. Generating Simulated NDVI Time-Series Data

Because true NDVI time-series data are unavailable, we generated the simulated NDVI time-series data in 2020 for the experiments of quantitative assessments. Specifically, we first generated a reference NDVI time series for each pixel by averaging all valid (cloud/snow-free) NDVI values at the same DOY during multiple years (2001–2020). If the number of valid NDVI values at a DOY was less than four, the NDVI value at this DOY in the reference VI time series was temporally linear interpolated. The reference NDVI time series of a pixel was thus regarded as the truth NDVI time series of this pixel, as graphically illustrated in Fig. 4. We then simulated missing values and NDVI noise in the reference NDVI time series according to the NDVI data quality layer in 2020. The NDVI data in the reference NDVI time series were assumed to be missing at the dates labeled as contamination (see light blue bar in Fig. 4). For a date labeled as uncertain data (reference to as "uncertain dates"), it is difficult to use the NDVI values at uncertain dates in 2020 to directly replace the corresponding values in the reference NDVI time series due to vegetation growth differences between the reference and the NDVI time series in 2020. Therefore, we followed [26] to establish the linear transfer function between the reference and the NDVI time series in 2020 for each pixel based on good quality NDVI observations and then modified the NDVI values at uncertain dates in 2020 using the established function. Considering negatively biased noise characteristics, the smaller values between the modified uncertain NDVI values and the values at the corresponding dates in the reference NDVI time series were used to generate the final simulated NDVI time-series data (see light green bar in Fig. 4). To reduce simulation uncertainty, we excluded those pixels with the number of good quality observations smaller than 5 or with low correlation coefficients of the linear transfer function (<0.85). Using multiyear MODIS NDVI data to composite reference NDVI time-series data has been widely adopted for quantitative assessments in relevant studies.

D. Determining Vegetation Phenological Characteristics

We designed two scenarios to examine the simulation of vegetation phenological characteristics in the NDVI time-series data. The first scenario is to simulate the local low VI values caused by winter wheat harvest at the site of North China Plain. The second scenario is to extract GOD and DOD from the NDVI time-series data. Specifically, we first applied the three SG-based methods to smooth NDVI time-series data and then fit the smoothed NDVI time series by the logistic function. GOD and DOD were determined to be the dates corresponding to the first local maximum (GOD) and the last local minimum (DOD) rates of change in curvature of the logistic-fit curve (see Zhang et al. [2, Fig. 2]).

IV. Results

A. Spatiotemporal Parameters Determination in iSTSG

iSTSG has two key parameters that need to be determined: the size of half temporal window [i.e., tw in (1)] and the

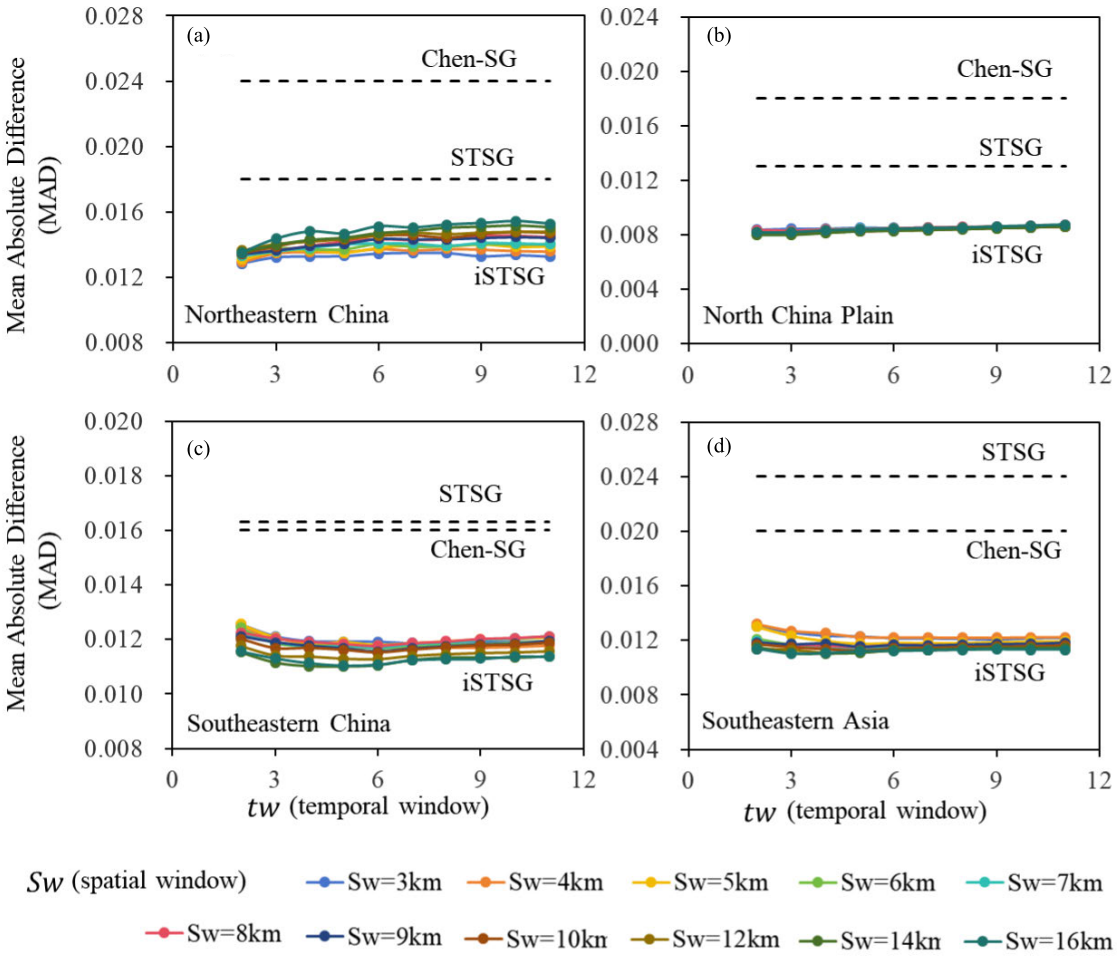

Fig. 5. Performance of iSTSG under different sizes of half temporal and spatial windows at different testing sites (a) Northeastern China, (b) North China Plain, (c) Southeastern China, and (d) Southeastern Asia. tw indicates the size of half temporal window and varies from 2 to 11, and sw indicates the size of half spatial window and varies from 3 to 16 km. For comparisons, the performance of Chen-SG and STSG methods was included in each panel (the black dashed lines).

size of half spatial window (i.e., sw in Fig. 2). We performed parameter sensitivity analyses by applying iSTSG to 1000 random pixels at each testing site while varying tw and sw. This experiment was conducted using the simulated NDVI time-series data. Under different combinations of tw and sw, we calculated MADs between the smoothed NDVI time series and the reference NDVI time series. tw varies from 2 to 11 at an interval of 1, and sw varies from 3 to 16 km. The experimental results show that the variations in MAD of iSTSG caused by the changes in tw or sw are relatively small compared with the MAD of Chen-SG and STSG methods (Fig. 5). For example, the MAD of iSTSG varies little with tw except for slightly higher MAD at small tw in the Southeastern China and Southeastern Asia [Fig. 5(c) and (d)]. The two sites are in tropical and subtropical areas with high cloud coverages, and small tw may lead to the failure in the generations of initial VI values by (1), which may explain the change patterns of the MAD of iSTSG at the two sites. In summary, the parameter sensitive experiment suggests that tw and sw may not need to be strictly selective and can be determined in a wide range of values, indicating the robustness of the new method. Considering computation efficiency and stability, we recommend the value of 4 for tw and 5 km for sw. In our sensitivity analysis, we considered different vegetation types (i.e., deciduous and evergreen vegetation, and crops) as well as regions with varying cloud coverages. However, the recommended parameters may need adjustment for extreme cloudy areas. For example, in some parts of Amazon forests, cloud is spatially continuous, and cloud-contaminated VI values may persist for months [27]. In such extreme scenarios, larger tw and sw may be necessary.

B. Visual Comparisons for the Reconstructed NDVI Images and Time-Series Data

Figs. 6 and 7 show the regional NDVI images reconstructed by the Chen-SG, STSG, and iSTSG methods at four testing sites. In general, the following two observations can be summarized.

1) Ability to Preserve Vegetation Phenological Characteristics: Compared with the Chen-SG and STSG methods, the iSTSG method better simulates some key vegetation phenological characteristics, evident from the results at the sites of Northeastern Asia [Fig. 6(a)] and North China Plain [Fig. 6(b)]. At the Northeastern Asia site, the NDVI time-series data simulated by iSTSG better preserved the greenup onset

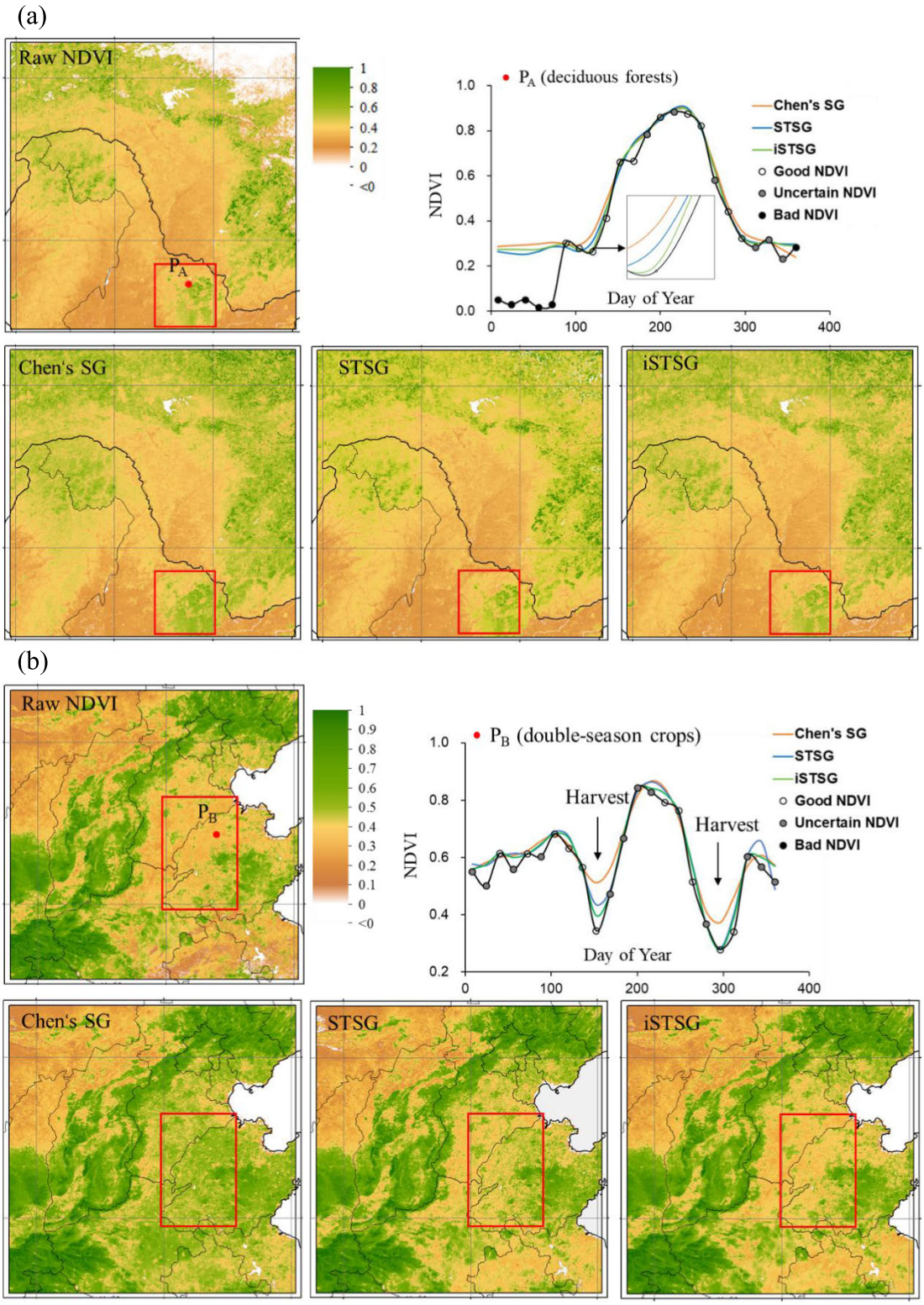

Fig. 6. Visual comparisons among the three SG-based methods at the sites of (a) Northeastern Asia and (b) North China Plain. In each panel, we show the raw NDVI image at a selected date and the NDVI images reconstructed by the Chen-SG, STSG, and iSTSG methods. Some differences in the reconstructed NDVI images among methods were highlighted by red rectangles. Moreover, an example of the reconstructed NDVI time-series data by the three SG-based methods is included in each panel.

characteristic of deciduous forests, whereas this phenological characteristic was erroneously detected at earlier dates using the NDVI time series simulated by Chen-SG and STSG methods [see the example of the NDVI time-series data of deciduous forests in Fig. 6(a)]. The reconstructed NDVI images on April 22, 2020, which is close to the

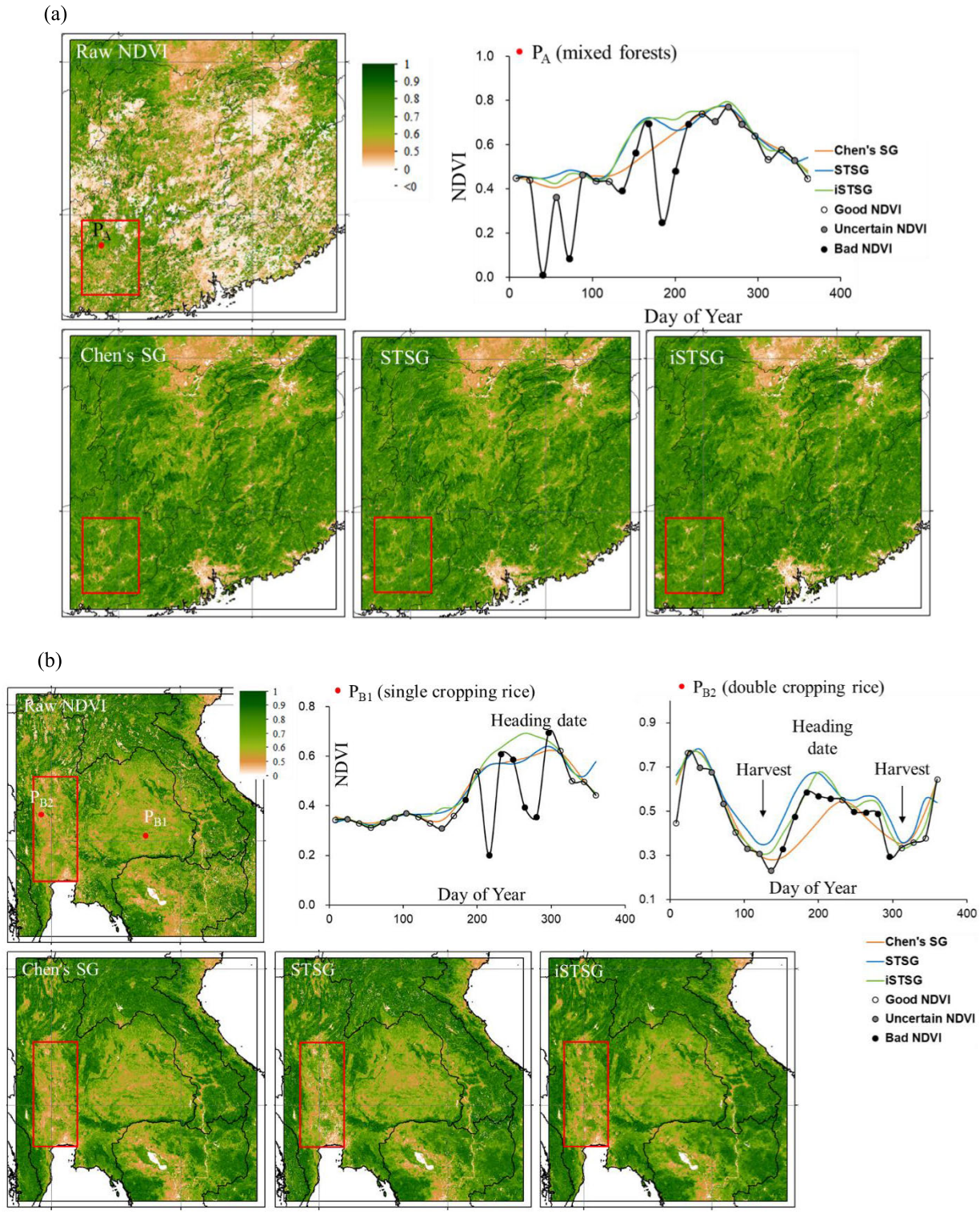

Fig. 7. Visual comparisons among the three SG-based methods at the sites of (a) Southeastern China and (b) Southeastern Asia. Some differences in the reconstructed NDVI images among methods were highlighted with red rectangles, and an example of the reconstructed NDVI time-series data for the three SG-based methods is shown in each panel.

GOD of deciduous forests, show that vegetation greenness of deciduous forests is slightly lower for iSTSG than that for Chen-SG and STSG [see the areas highlighted by rectangles in Fig. 6(a)], suggesting later iSTSG-derived GOD. This observation was further confirmed by extracting phenology from the reconstructed NDVI time-series data (details were given in Section IV-D).

At the North China Plain site with double-season crops (winter wheat and corn), we showed the reconstructed NDVI images on June 9, 2020, which is close to the harvest date

TABLE I
MADs Between the Smoothed NDVI Time Series and Reference NDVI Time Series Averaged Over Each Testing Site. Moreover, an Ablation Experiment Was Included to Show the Effectiveness of Each Step of iSTSG

	Northeastern Asia	North China Plain	Southeastern China	Southeastern Asia	**Average**
Chen-SG	0.024	0.018	0.016	0.020	0.020
STSG	0.018	0.013	0.016	0.024	0.018
iSTSG	0.015	0.008	0.012	0.012	**0.012**
Ablation experiment					
iSTSG_S1	0.017	0.010	0.014	0.015	0.014
iSTSG_S2	0.019	0.015	0.013	0.014	0.015

of winter wheat [Fig. 6(b)]. Compared with Chen-SG and STSG, the iSTSG method better preserved the harvest phenological characteristics. For example, the low NDVI values due to winter wheat harvest were erroneously raised by using Chen-SG and STSG [see the areas highlighted by rectangles in Fig. 6(b)], with more serious overcorrections observed in the Chen-SG method. Thus, it greatly underestimated the depth of curve valley during May and June in the reconstructed NDVI time-series data.

2) Ability to Reconstruct Temporally Continuous Missing Values: It can be observed that continuous missing values in the NDVI time series can only be reconstructed by the spatiotemporal filters STSG and iSTSG, with iSTSG showing more stable performance than STSG (Fig. 7). For instance, temporally continuous missing values occurred in the rainy season (May–October) at the site of southeastern Asia [Fig. 7(b)]. In Thailand, rice takes about 1–2 months to reach the heading date (approximately the date with the maximum NDVI) after planting in the rainy season and is then harvested at the time 2–3 months after rice heading ([28]). For single cropping rice, the NDVI time series generated by Chen-SG and STSG were obviously incorrect with too late rice heading dates, whereas the iSTSG-derived NDVI time series are more reasonable [point PB1 in Fig. 7(b)]. For double cropping rice [point PB2 in Fig. 7(b)], it is too long for the time interval between rice planting and heading in the NDVI time series generated by the Chen-SG method, which is caused by the temporally continuous cloud-contaminated NDVI data in the rainy season after rice planting. Visual comparisons of reconstructed NDVI images at the four testing sites suggest the strengths of iSTSG in the removal of NDVI noise, preservations of vegetation phenology, and processing of temporally continuous missing NDVI data (Figs. 6 and 7).

C. Quantitative Assessments Based on Simulated NDVI Time-Series Data

We conducted quantitative assessments based on the simulated NDVI time-series data (see Section III-C for simulation details). Table I summarizes the MAD values between the reconstructed NDVI time series and reference NDVI time series for the three SG-based methods (for the MAD values at the pixel level, please refer to Fig. 8). We found that the iSTSG method performed the best with the smallest MAD values, followed by the STSG and Chen-SG methods. The MAD values averaged over the four testing sites are 0.012, 0.018, and 0.020 for the iSTSG, STSG, and Chen-SG methods, respectively (Table I). In addition, the STSG method has smaller MAD values than the Chen-SG method except for the site of southeastern Asia. STSG employs multiyear NDVI time-series data, whereas there were substantial land cover changes over the years due to intense human activity in southeastern Asia, which may explain the worst performance of STSG at this site. This experiment confirmed that the proposed iSTSG method improves fidelity in reconstructed NDVI values over previous SG-based methods.

Given that iSTSG consists of two steps, we further tested the effectiveness of each step by designing an ablation experiment. Two scenarios were specifically investigated. In the first scenario, we replaced the first step of iSTSG with the operation of linear interpolation, which tested the effectiveness to incorporate spatiotemporal information to initially fill missing values in the VI time series (referred to as iSTSG_ S1). In the second scenario, we replaced the second step of iSTSG with the iterative SG filter proposed by Chen-SG (referred to as iSTSG_ S2). Results show the decreased MAE values when either of the two steps of iSTSG was replaced (Table I). As we expected, iSTSG_ S1 has poor performance than iSTSG_ S2 at the cloudy sites of Southeastern China and Southeastern Asia, suggesting the necessity to incorporate spatiotemporal information to fill continuous missing VI values. In contrast, iSTSG_ S2 performed obviously worse than iSTSG_ S1 at the site of North China Plain, which can be attributed to the poor simulations of crop harvest phenological characteristics using the iterative SG filter in iSTSG_ S2.

D. Simulation of Vegetation Phenological Characteristics

The NDVI time-series data provide key vegetation phenological information. We expect that iSTSG can better simulate vegetation phenological characteristics in the NDVI time-series data, which was evaluated in two scenarios.

In the first scenario, we examined the preservation of local low VI values caused by winter wheat harvest at the site of North China Plain. In specific, we first identified wheat pixels in the North China Plain using the identification algorithm proposed by Qiu et al. [29]. To reduce uncertainty, only those pixels continuously planted by winter wheat during 2008–2020 were included. We applied the three SG-based methods to the simulated NDVI time-series data and calculated the MAD between the smoothed NDVI value and the reference NDVI value at 161 DOY (approximately the date after wheat

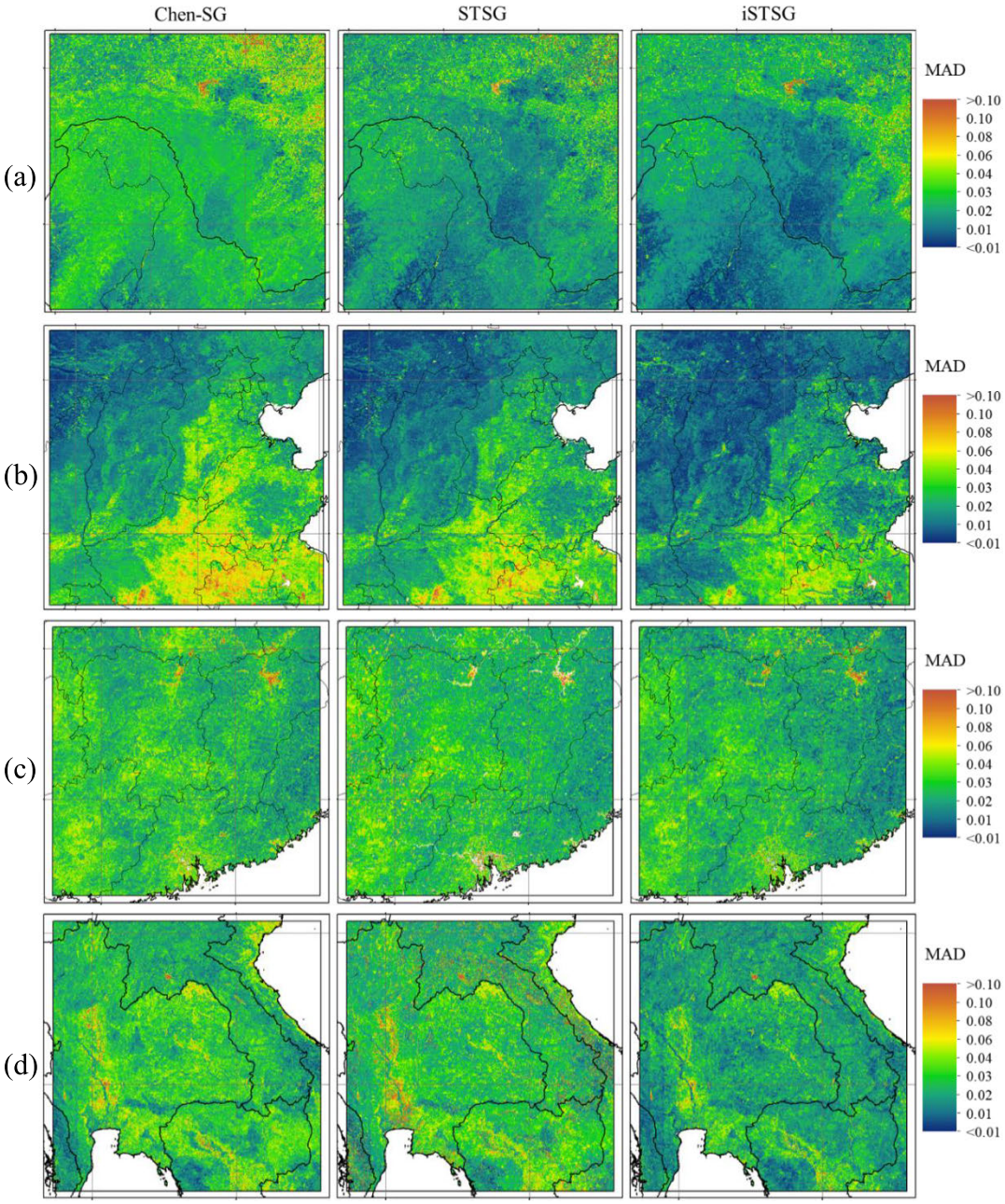

Fig. 8. Spatial distributions of the MADs between the smoothed NDVI time series and reference NDVI time series for the three SG-based methods. (a) Northeastern Asia. (b) North China Plain. (c) Southeastern China. (d) Southeastern Asia.

harvest) for each wheat pixel. Results show that iSTSG achieved smaller MAD values at 161 DOY than the comparing methods. The regional averaged MAD values for iSTSG, STSG, and Chen-SG are 0.020 versus 0.045 versus 0.132, respectively (Fig. 9), suggesting better simulations of wheat harvest phenological characteristics by the iSTSG method.

In the second scenario, we examined the performance to extract GOD and DOD from the smoothed NDVI time-series data. We conducted this experiment at the site of Northeastern Asia, which is mainly covered by forests with obvious annual greenness changes. The two cropland sites (North China Plain and Southeastern Asia) were excluded from this analysis because crops have different phenological definitions [30]. The site of Southeastern China was also excluded due to the main coverage of evergreen vegetation. The lack of vegetation greenness seasonality could decrease phenological detection accuracy and thereby confuse the analyses. In this experiment, we first used the three SG-based methods to smooth the real NDVI time-series data in 2020 and detected GOD and DOD for each pixel except nonvegetated and crop pixels in Northeastern Asia (screen out using the land cover product MCD12Q1). Based on the illustrations in Fig. 1, we anticipated that iSTSG would produce later GOD and earlier DOD values compared to the other two methods. The results confirmed our expectations: the mean GOD values are 104.2, 109.6, and 112.5 DOY, and the mean DOD values are

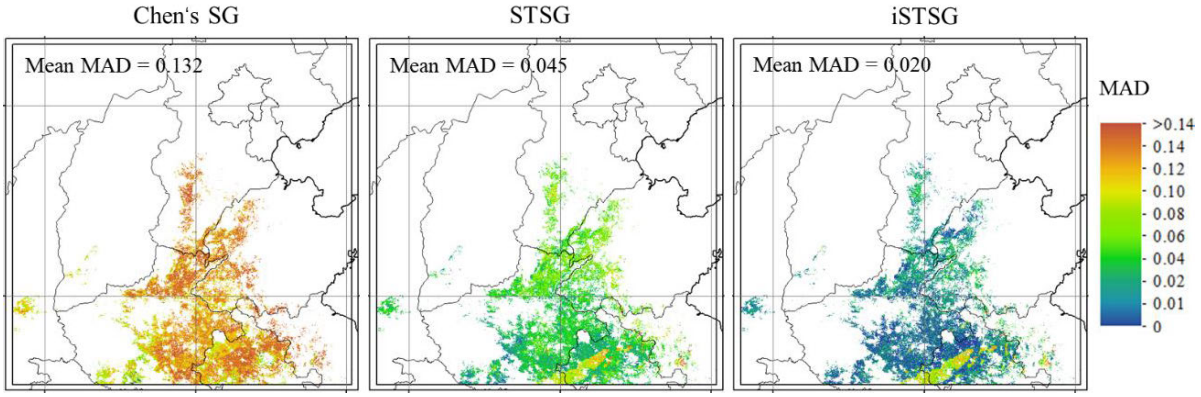

Fig. 9. MADs between the reconstructed NDVI and reference NDVI values at 161 DOY (approximately the date after winter wheat harvest) for the winter wheat pixels in the North China Plain. This analysis was based on the simulated MODIS NDVI time-series data. To reduce uncertainty, only those pixels continuously planted by winter wheat during 2008–2020 were included.

296.0, 292.7, and 292.1 DOY for Chen-SG, STSG, and iSTSG, respectively (Fig. 10). We further applied the three SG-based methods to the simulated NDVI time-series data and calculated the differences between the true and estimated GOD (or DOD) values (referred to as GOD-d and DOD-d, Fig. 11). The results revealed that Chen-SG generated significantly advanced GOD estimates (i.e., positive GOD-d) and delayed DOD estimates (i.e., negative DOD-d), highlighting its limitations for vegetation phenological applications. In contrast, iSTSG effectively addressed this systematical error and achieved the smallest GOD-d and DOD-d values among the three methods. The mean GOD-d (DOD-d) values for Chen-SG, STSG, and iSTSG are 5.2, 2.0, and 1.1 days (−2.8, −0.4, and 0.3 days), respectively (Fig. 11).

V. Discussion

A. Improvements in iSTSG

The MODIS NDVI time-series data are among the most widely used remote sensing data. There is significant interest in improving the quality of NDVI time-series data. Considering the negatively biased noise characteristic in the NDVI time-series data, the principle of approaching the upper envelope of NDVI time-series data has been widely adopted in previous smooth filters (e.g., SG by Chen et al. [7], Whittaker filter by Atzberger and Eilers [11], and HANTs by Zhou et al. [8]). However, two concerns still remain for the processed NDVI time-series data. One is continuous missing values in the MODIS NDVI time-series data. For this problem, several recent methods have incorporated multiyear spatiotemporal information to reconstruct temporally continuous missing NDVI data (e.g., STSG by Cao et al. [18] and ST-Tensor by Chu et al. [19]). However, uncertainties arise from possible inconsistency in the NDVI time-series data among different years. Our experiments showed that STSG performed even worse than Chen-SG at the cloudy site of Southeastern Asia (MAD: 0024 versus 0.020; Table I), which may be explained by interannual differences in rice cultivation caused by climates and agricultural management. Instead, iSTSG uses spatiotemporal NDVI data in the current year only and estimates the relationship of NDVI values among different dates based on autocorrelation of MODIS NDVI time-series data (2). In our experiments, iSTSG also demonstrated its effectiveness in regions with less distinct seasonality (e.g., southeastern China). For evergreen vegetation, we assume that the NDVI value at any given date can be reliably estimated from those NDVI values at other dates within a temporal window because of the small annual variations in greenness. To confirm this assumption, we evaluated the goodness of linear fit for initial NDVI estimates (i.e., the equation shown in Fig. 3) at the four testing sites. The standard error of linear regressions, averaged over all dates, was found to be comparable across testing sites, with error values ranging from 0.027 to 0.033. This suggests the applicability of iSTSG for vegetation with minimal seasonality. The incorporation of spatiotemporal information makes iSTSG applicable for filling continuous missing values in the NDVI time-series data [Fig. 7(a) and (b)]. We also compared iSTSG with other methods besides the SG-based methods. Specifically, we compared iSTSG with the HANT method [8] and the results further confirm the superiority of the new method (Table S1 in Supplementary Materials). Another concern regarding previous methods is the overcorrection of true local low values in the process of approaching the upper envelope of NDVI time-series data. Some vegetation phenological stages, such as GOD, DOD, and crop harvest stages, occur near the date with local low NDVI values; thus, these phenological characteristics may be poorly simulated in the smoothed NDVI time-series data (Fig. 1). To address this issue, iSTSG considers the shapes of NDVI time series in the local segments and propose an indicator to quantify possible overcorrections in the NDVI time series (4). Our experiments confirmed that the systematic error in phenology estimates of Chen-SG (i.e., earlier GOD and later DOD) has been effectively corrected when using iSTSG (Figs. 10 and 11).

Because of the two improvements in iSTSG, we expect that the new method can benefit many applications of MODIS NDVI time series. More accurate reconstruction of continuous missing NDVI data is important for vegetation productivity estimates [31]. Better preservation of crop harvest

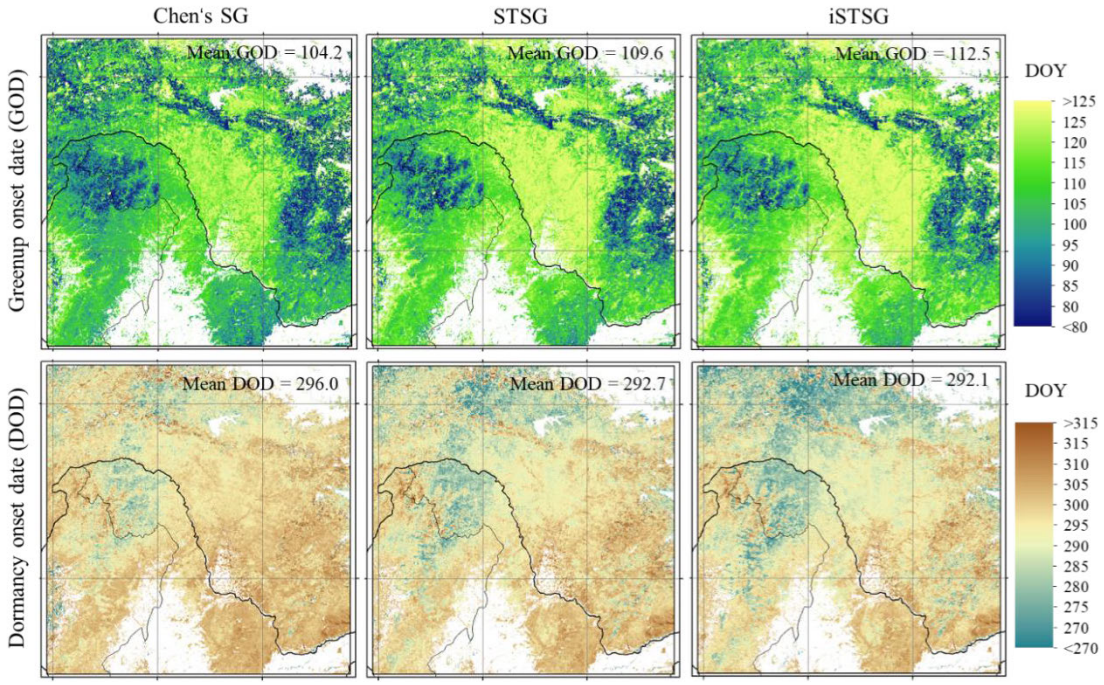

Fig. 10. GOD and DOD in 2020 at the site of Northeastern Asia, which estimated from the NDVI time-series data smoothed by the Chen-SG, STSG, and iSTSG methods. Nonvegetated pixels and croplands were excluded from this analysis.

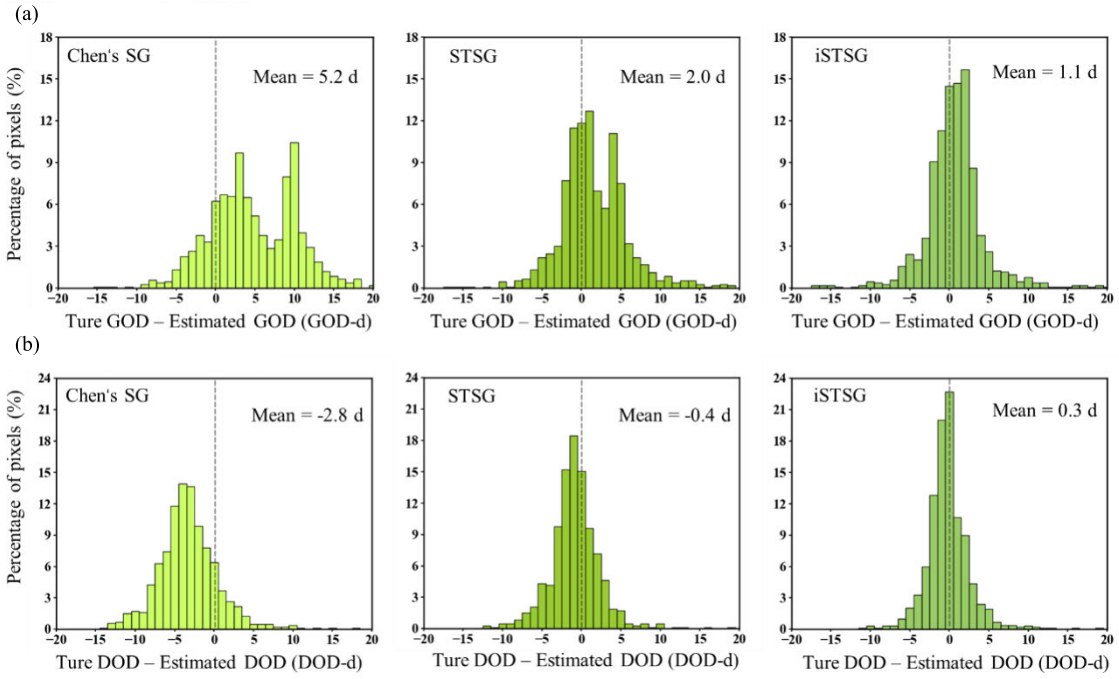

Fig. 11. Differences between true phenological dates and estimated phenological dates based on the simulated NDVI time-series data in 2020 at the site of Northeastern Asia. (a) GOD. (b) DOD.

characteristics can improve cropping intensity monitoring (i.e., the number of growth cycles per year) and crop mapping [32]. As important vegetation phenological stages, GOD and DOD have been mostly investigated in previous phenology studies. Our study highlights uncertainty in GOD and DOD estimates caused by curve smoothing operations and suggests a particular application of iSTSG in future vegetation/crop phenology studies.

B. Applicability of iSTSG to Other Satellite VIs and Computation Efficiency

For the practical applications of iSTSG, users may be particularly interested in the following aspects. First, except for the MODIS NDVI time-series data in our experiments, whether iSTSG can be applied to the MODIS EVI time-series data? Here, we performed the quantitative assessment experiment again (i.e., the experiment in Section IV-C) but for

the EVI time-series data provided by the MOD13A2 product. The results show that the MAD values averaged over the four testing sites are 0.016, 0.021, and 0.011 for Chen-SG, STSG, and iSTSG, respectively (Table S2 in Supplementary Materials), suggesting the superiority of iSTSG in reconstructing MODIS EVI time-series data compared to previous SG-based methods. It is interesting to note that STSG performed even worse than Chen-SG for MODIS EVI time-series data. Unlike NDVI, EVI has a nonratio form and is thus more sensitive to different kinds of noise (e.g., atmospheric conditions and terrain), which leads to larger data inconsistency over the years. This may be the reason to be responsible for the poor performance of STSG.

Second, MODIS has provided data for more than 20 years and is entering the period of end of life [33]. As the successor of MODIS, the VIIRS instrument on the Suomi National Polar-orbiting Partnership provides VI product (VNP13A1) with a 16-day acquisition period at 500-m spatial resolution. Here, we tested the applicability to VIIRS NDVI and EVI time-series data with the quantitative assessment experiment again. Experimental results confirm the smallest MAD values for the iSTSG method (Table S3 in Supplementary Materials), highlighting the potential of iSTSG to process VIIRS NDVI/EVI time-series data after the era of MODIS.

Third, computation efficiency may be a concern in practical applications. As the planetary-scale geospatial analysis platform, GEE has a rich satellite data catalog, including MODIS and VIIRS, and realized geospatial processing by the google cloud platform, which greatly popular large-scale remote sensing applications [34]. Therefore, we programmed the three SG-based methods on GEE and tested the processing time to process the MODIS NDVI time-series data. As we expected, Chen-SG does not include spatial computation (i.e., spatial window) and thus has the highest computation efficiency with about 6.5 min to process an area of 1000 × 1000 km (Table II). Compared with STSG, which uses multiyear data, iSTSG improved computational efficiency by nearly eight times (20.0 versus 152.8 min for 1000 × 1000 km). Furthermore, one may be concerned whether the computation efficiency of the new method deteriorates rapidly when applied to larger areas, a phenomenon known as "computation efficiency scalability" [27]. To address this concern, we tested the processing times when applying the methods to areas of different sizes (i.e., from 500 × 500 to 3000 × 3000 km, Fig. S2). The STSG method was excluded from this experiment due to its noticeably lower computation efficiency (Table II). Results showed that, as area sizes increased, iSTSG exhibited a similar linear increase in processing time as the Chen-SG method (Fig. 12), suggesting that iSTSG maintains good computation efficiency scalability. Considering the balance between reconstruction accuracy and computation efficiency, iSTSG has great potential to be applied at regional and continental scales.

TABLE II

COMPUTATION EFFICIENCY OF DIFFERENT METHODS ON THE GEE. THE AREA AT EACH TESTING SITE IS ABOUT 1000 × 1000 KM

Processing time (Unit: minute)	Chen-SG	STSG	iSTSG
Northeastern Asia	5	140	21
North China Plain	7	165	22
Southeastern China	5	136	16
Southeastern Asia	9	170	19
Average	6.5	152.8	20.0

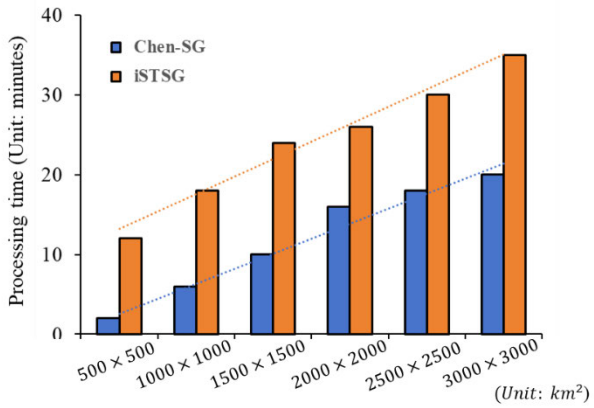

Fig. 12. Time required to reconstruct MODIS NDVI time-series data for areas of different sizes. The dashed lines indicate the linear trends of processing time. The STSG method was excluded due to its significantly lower computation efficiency.

C. Uncertainties of iSTSG

Some uncertainties of iSTSG should be clarified. Because the MODIS VI product is temporally composited (e.g., 16 days for MOD13A2), one may be concerned that disparate dates within a composited period could be chosen between the target pixel and the neighboring pixels. Although the maximum difference in acquisition time between two pixels is theoretically 16 days for MOD13A2, the actual time difference, averaged over mainland China, was examined in a previous study and was found to be only 2.2 days (see Cao et al. [18, Fig. S6]). We expect that NDVI/EVI varies little within this short period and thus less affects iSTSG.

Another concern is the applicability of iSTSG in regions with highly dynamic land cover changes, such as deforested areas or those affected by bushfires. It may be challenging to predict NDVI values caused by land cover changes within the current year. However, iSTSG assumes spatial autocorrelation and utilizes neighboring similar pixels, which was found to be effective for reconstructing NDVI values of the target pixel when clouds are spatially discontinuous [18]. To address this, we conducted an additional experiment. In early 2020, bushfires were reported in the eastern regions of New South Wales and Victoria, Australia. It can be seen that the iSTSG method successfully captured the abrupt decreases in NDVI values caused by bushfires (Fig. 13). In areas covered by evergreen forests, the reconstructed NDVI values on December 9, 2019, were as high as 0.8, but by January 1, 2020, it had dropped to below 0.4 (see the lower panels in Fig. 13). These results indicate that iSTSG can be applied to the regions with land cover changes occurring within the current year. However,

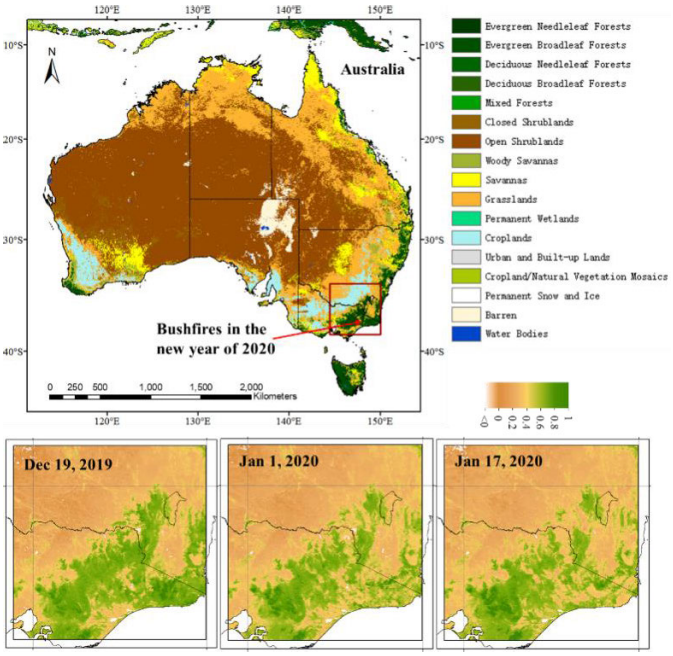

Fig. 13. (Top) Land cover types in Australia. The red box indicates the areas affected by bushfires in early 2020. (Bottom) NDVI values reconstructed by iSTSG at different dates.

care should be taken when using iSTSG in areas where very small-scale land cover changes, as it may be difficult to rely on neighboring pixel information in such cases.

In extremely cloudy areas, it may be difficult to generate the initial VI values due to spatially and temporally continuous missing values (i.e., step 1 in iSTSG). For these cases, iSTSG fills the missing VI values by linear interpolation. To quantify this kind of situation, we selected the cloudy Southeastern Asia as the example and calculated the percentage of pixels. Results show that the linear-interpolated pixels account for about 12.5% of total pixels in this cloudy region, suggesting that missing values in most pixels can be filled by iSTSG (Fig. S1 in Supplementary Materials). The percentage is expected to be further reduced by using higher spatiotemporal MODIS and VIIRS product (e.g., MOD09A1 product with 500-m and 8-day resolution). Besides, we observed that some linear-interpolated pixels are distributed in coastal zones or near inland lakes (Fig. S1). For vegetation pixels near ocean or lakes, it is more difficult to search similar pixels in spatial windows, which may partly explain this observed spatial distribution.

It is challenging to apply iSTSG to medium spatial resolution VI time-series data (e.g., 30-m Landsat and 10-m Sentinel-2). Low temporal resolution of Landsat and Sentinel-2 data makes the VI time-series data rather discontinuous. In cloudy areas, cloud-free Landsat observations are often few with uneven temporal distribution in a year [35]. Currently, reconstructing continuous Landsat or Sentinel-2 VI time-series data is mainly based on multisource data fusion technology, such as MODIS-Landsat spatiotemporal data fusion [26] or the fusion of synthetic aperture radar (SAR) and optical VI data [36], [37].

For some specific applications, high-quality VI time-series data need to be generated in real time, such as for crop growth monitoring. For instance, real-time VI time-series data are crucial for in-season crop phenology detection [38]. iSTSG can be employed to generate initial VI estimates in real time using only the VI values in the left-haft window before the prediction date (i.e., the first step in iSTSG). However, smoothing the VI time series with the iterative SG filter still requires several VI observations after the prediction date (i.e., the second step in iSTSG). Some recent studies have focused on predicting VI values after a given date using historical VI data [38], [39]. The integration of VI predictions with iSTSG for generating high-quality real-time VI time-series data could be an avenue for further research.

VI. Conclusion

Reconstructing the MODIS and its successor, VIIRS NDVI/EVI time-series data have broad interests. In this study, we proposed an improved iSTSG method with two main improvements. The first improvement is to better simulate vegetation phenological characteristics at some key stages in the reconstructed NDVI time series. In previous methods, the principle of approaching upper envelope of NDVI time series may cause overcorrections on some true local low NDVI values. iSTSG addressed this issue by automatically quantifying possible overcorrections in the NDVI time series and making the corresponding adjustments. The experimental results, based on the real and simulated NDVI time series, showed that GOD and DOD were extracted more accurately in the NDVI time series reconstructed by iSTSG than that by previous SG-based methods (e.g., the MAD values of GOD are 5.2, 2.0, and 1.1 days achieved by Chen-SG, STSG, and iSTSG, respectively; Fig. 11). The second improvement in iSTSG is to fill missing values in the NDVI time series by considering autocorrelation of the VI time series, which enable the new method to be applicable to the NDVI time series with temporally continuous missing values. In particular, iSTSG requires NDVI time series in the current year only and thus has more stable performance than the previous STSG method that requires multiyear historical NDVI data. Moreover, iSTSG has a good balance between reconstruction accuracy and computation efficiency. The source codes of iSTSG (GEE version and Python version) are available from https://github.com/wyWang365/iSTSG.

References

[1] R. B. Myneni et al., "Global products of vegetation leaf area and fraction absorbed PAR from year one of MODIS data," *Remote Sens. Environ.*, vol. 83, nos. 1–2, pp. 214–231, 2002.

[2] X. Zhang et al., "Monitoring vegetation phenology using MODIS," *Remote Sens. Environ.*, vol. 84, no. 3, pp. 471–475, Mar. 2003.

[3] M. A. Friedl et al., "MODIS collection 5 global land cover: Algorithm refinements and characterization of new datasets," *Remote Sens. Environ.*, vol. 114, no. 1, pp. 168–182, Jan. 2010.

[4] B. N. Holben, "Characteristics of maximum-value composite images from temporal AVHRR data," *Int. J. Remote Sens.*, vol. 7, no. 11, pp. 1417–1434, Nov. 1986.

[5] J. N. Hird and G. J. McDermid, "Noise reduction of NDVI time series: An empirical comparison of selected techniques," *Remote Sens. Environ.*, vol. 113, no. 1, pp. 248–258, Jan. 2009.

[6] S. Li, L. Xu, Y. Jing, H. Yin, X. Li, and X. Guan, "High-quality vegetation index product generation: A review of NDVI time series reconstruction techniques," *Int. J. Appl. Earth Observ. Geoinf.*, vol. 105, Dec. 2021, Art. no. 102640.

[7] J. Chen, P. Jonsson, M. Tamura, Z. H. Gu, B. Matsushita, and L. Eklundh, "A simple method for reconstructing a high-quality NDVI time-series data set based on the Savitzky-Golay filter," *Remote Sens. Environ.*, vol. 91, nos. 3–4, pp. 332–344, Jun. 2004.

[8] J. Zhou, L. Jia, and M. Menenti, "Reconstruction of global MODIS NDVI time series: Performance of harmonic ANalysis of time series (HANTS)," *Remote Sens. Environ.*, vol. 163, pp. 217–228, Jun. 2015.

[9] Y. Julien and J. A. Sobrino, "Comparison of cloud-reconstruction methods for time series of composite NDVI data," *Remote Sens. Environ.*, vol. 114, no. 3, pp. 618–625, Mar. 2010.

[10] W. Zhu, Y. Pan, H. He, L. Wang, M. Mou, and J. Liu, "A changing-weight filter method for reconstructing a high-quality NDVI time series to preserve the integrity of vegetation phenology," *IEEE Trans. Geosci. Remote Sens.*, vol. 50, no. 4, pp. 1085–1094, Apr. 2012.

[11] C. Atzberger and P. H. C. Eilers, "A time series for monitoring vegetation activity and phenology at 10-daily time steps covering large parts of south America," *Int. J. Digit. Earth*, vol. 4, no. 5, pp. 365–386, Sep. 2011.

[12] P. S. A. Beck, C. Atzberger, K. A. Høgda, B. Johansen, and A. K. Skidmore, "Improved monitoring of vegetation dynamics at very high latitudes: A new method using MODIS NDVI," *Remote Sens. Environ.*, vol. 100, no. 3, pp. 321–334, Feb. 2006.

[13] P. Jonsson and L. Eklundh, "Seasonality extraction by function fitting to time-series of satellite sensor data," *IEEE Trans. Geosci. Remote Sens.*, vol. 40, no. 8, pp. 1824–1832, Aug. 2002.

[14] G. J. Roerink, M. Menenti, and W. Verhoef, "Reconstructing cloudfree NDVI composites using Fourier analysis of time series," *Int. J. Remote Sens.*, vol. 21, no. 9, pp. 1911–1917, Jan. 2000.

[15] X. Lu, R. Liu, J. Liu, and S. Liang, "Removal of noise by wavelet method to generate high quality temporal data of terrestrial MODIS products," *Photogramm. Eng. Remote Sens.*, vol. 73, no. 10, pp. 1129–1139, Oct. 2007.

[16] P. M. Atkinson, C. Jeganathan, J. Dash, and C. Atzberger, "Inter-comparison of four models for smoothing satellite sensor time-series data to estimate vegetation phenology," *Remote Sens. Environ.*, vol. 123, pp. 400–417, Aug. 2012.

[17] R. Liu, R. Shang, Y. Liu, and X. Lu, "Global evaluation of gap-filling approaches for seasonal NDVI with considering vegetation growth trajectory, protection of key point, noise resistance and curve stability," *Remote Sens. Environ.*, vol. 189, pp. 164–179, Feb. 2017.

[18] R. Cao et al., "A simple method to improve the quality of NDVI time-series data by integrating spatiotemporal information with the Savitzky–Golay filter," *Remote Sens. Environ.*, vol. 217, pp. 244–257, Nov. 2018.

[19] D. Chu et al., "Long time-series NDVI reconstruction in cloud-prone regions via spatio-temporal tensor completion," *Remote Sens. Environ.*, vol. 264, Oct. 2021, Art. no. 112632.

[20] S. Li et al., "Monitoring vegetation dynamics (2010–2020) in shengnongjia forestry district with cloud-removed MODIS NDVI series by a spatio-temporal reconstruction method," *Egyptian J. Remote Sens. Space Sci.*, vol. 26, no. 3, pp. 527–543, Dec. 2023.

[21] A. Savitzky and M. J. E. Golay, "Smoothing and differentiation of data by simplified least squares procedures," *Anal. Chem.*, vol. 36, no. 8, pp. 1627–1639, Jul. 1964.

[22] X. Liu, H. Shen, Q. Yuan, X. Lu, and S. Li, "One-step high-quality NDVI time-series reconstruction by joint modeling of gradual vegetation change and negatively biased atmospheric contamination," *IEEE Trans. Geosci. Remote Sens.*, vol. 60, 2022, Art. no. 4407017, doi: 10.1109/TGRS.2021.3124798.

[23] X. Yang, J. Chen, Q. Guan, H. Gao, and W. Xia, "Enhanced spatial–temporal Savitzky–Golay method for reconstructing high-quality NDVI time series: Reduced sensitivity to quality flags and improved computational efficiency," *IEEE Trans. Geosci. Remote Sens.*, vol. 60, 2022, Art. no. 4412317.

[24] J. Tian et al., "Improving the accuracy of spring phenology detection by optimally smoothing satellite vegetation index time series based on local cloud frequency," *ISPRS J. Photogramm. Remote Sens.*, vol. 180, pp. 29–44, Oct. 2021.

[25] K. Didan, "MODIS/Terra vegetation indices 16-day L3 global 1km SIN grid V061," NASA EOSDIS Land Processes Distributed Active Archive Center, 2021, doi: 10.5067/MODIS/MOD13A2.061.

[26] Y. Chen, R. Cao, J. Chen, L. Liu, and B. Matsushita, "A practical approach to reconstruct high-quality Landsat NDVI time-series data by gap filling and the Savitzky–Golay filter," *ISPRS J. Photogramm. Remote Sens.*, vol. 180, pp. 174–190, Oct. 2021.

[27] R. Cao, Y. Chen, J. Chen, X. Zhu, and M. Shen, "Thick cloud removal in Landsat images based on autoregression of Landsat time-series data," *Remote Sens. Environ.*, vol. 249, Nov. 2020, Art. no. 112001.

[28] S. Suwannachatkul, T. Kasetkasem, K. Chumkesornkulkit, P. Rakwatin, T. Chanwimaluang, and I. Kumazawa, "Rice cultivation and harvest date identification based on a hidden Markov model," in *Proc. 11th Int. Conf. Electr. Eng./Electron., Comput., Telecommun. Inf. Technol. (ECTI-CON)*, May 2014, pp. 1–6.

[29] B. Qiu et al., "Winter wheat mapping combining variations before and after estimated heading dates," *ISPRS J. Photogramm. Remote Sens.*, vol. 123, pp. 35–46, Jan. 2017.

[30] T. Sakamoto, B. D. Wardlow, A. A. Gitelson, S. B. Verma, A. E. Suyker, and T. J. Arkebauer, "A two-step filtering approach for detecting maize and soybean phenology with time-series MODIS data," *Remote Sens. Environ.*, vol. 114, no. 10, pp. 2146–2159, Oct. 2010.

[31] P. Schubert et al., "Modeling GPP in the Nordic forest landscape with MODIS time series data—Comparison with the MODIS GPP product," *Remote Sens. Environ.*, vol. 126, pp. 136–147, Nov. 2012.

[32] M. Boschetti et al., "PhenoRice: A method for automatic extraction of spatio-temporal information on Rice crops using satellite data time series," *Remote Sens. Environ.*, vol. 194, pp. 347–365, Jun. 2017.

[33] M. O. Román et al., "Continuity between NASA MODIS collection 6.1 and VIIRS collection 2 land products," *Remote Sens. Environ.*, vol. 302, Mar. 2024, Art. no. 113963.

[34] N. Gorelick, M. Hancher, M. Dixon, S. Ilyushchenko, D. Thau, and R. Moore, "Google Earth engine: Planetary-scale geospatial analysis for everyone," *Remote Sens. Environ.*, vol. 202, pp. 18–27, Dec. 2017.

[35] L. Yan and D. P. Roy, "Spatially and temporally complete Landsat reflectance time series modelling: The fill-and-fit approach," *Remote Sens. Environ.*, vol. 241, May 2020, Art. no. 111718.

[36] Y. Mao, T. G. Van Niel, and T. R. McVicar, "Reconstructing cloud-contaminated NDVI images with SAR-optical fusion using spatio-temporal partitioning and multiple linear regression," *ISPRS J. Photogramm. Remote Sens.*, vol. 198, pp. 115–139, Apr. 2023.

[37] Y. Han, J. Huang, F. Ling, X. Gao, W. Cai, and H. Chi, "RDNRnet: A reconstruction solution of NDVI based on SAR and optical images by residual-in-residual dense blocks," *IEEE Trans. Geosci. Remote Sens.*, vol. 62, 2024, Art. no. 4402514, doi: 10.1109/TGRS.2024.3354255.

[38] R. Cao et al., "A spatiotemporal shape model fitting method for within-season crop phenology detection," *ISPRS J. Photogramm. Remote Sens.*, vol. 217, pp. 179–198, Nov. 2024.

[39] Y. Shen et al., "Developing an operational algorithm for near-real-time monitoring of crop progress at field scales by fusing harmonized Landsat and sentinel-2 time series with geostationary satellite observations," *Remote Sens. Environ.*, vol. 296, Oct. 2023, Art. no. 113729.

Weiyi Wang received the B.E. degree in spatial information and digital technology from the University of Electronic Science and Technology of China, Chengdu, China, in 2022, where she is currently pursuing the M.E. degree in surveying and mapping technology.

Her research interests include remote sensing image processing and vegetation parameter retrieval.

Ruyin Cao received the B.S. degree in resource science and engineering and the Ph.D. degree in geography from Beijing Normal University, Beijing, China, in 2007 and 2013, respectively.

From 2013 to 2015, he was a Post-Doctoral Fellow with the National Institute for Environmental Studies, Tsukuba, Japan. He is currently a Professor with the School of Resources and Environment, University of Electronic Science and Technology of China, Chengdu, China. His research interests include remote sensing image processing and vegetation parameter retrieval.

Licong Liu received the B.E. degree in spatial information and digital technology from the University of Electronic Science and Technology of China, Chengdu, China, in 2017, and the M.E. degree in geography from Beijing Normal University, Beijing, China, in 2020, where he is currently pursuing the Ph.D. degree in geography.

His research interests include remote sensing image processing and remote sensing modeling.

Ji Zhou (Senior Member, IEEE) received the B.S. degree in geographic information system from Nanjing University, Nanjing, China, in 2005, and the Ph.D. degree in geography from Beijing Normal University, Beijing, China, in 2010.

He was a Visiting Ph.D. Student at the Department of Geography, University of Western Ontario, London, ON, Canada, from 2008 to 2009. From 2015 to 2016, he was an International Research Fellow with European Space Agency, Rome, Italy. He is currently a Professor with the School of Resources and Environment, University of Electronic Science and Technology of China, Chengdu, China. His research focuses on thermal and passive microwave remote sensing of land surfaces.

Miaogen Shen received the B.S. degree in physics and the Ph.D. degree in physical geography from Beijing Normal University, Beijing, China, in 2004 and 2009, respectively.

He is currently a Professor with the State Key Laboratory of Earth Surface Processes and Resource Ecology, Beijing Normal University. His research interests include responses and feedback of terrestrial ecosystems to climate change, and ecological remote sensing, with a focus on plant phenology and the Tibetan Plateau.

Xiaolin Zhu (Senior Member, IEEE) received the B.Sc. degree in resource science and engineering and the M.Sc. degree in civil engineering from Beijing Normal University, Beijing, China, in 2007 and 2010, respectively, and the Ph.D. degree in geography from Ohio State University, Columbus, OH, USA, in 2014.

He was a Post-Doctoral Researcher with Colorado State University, Fort Collins, CO, USA, and the University of California at Davis, Davis, CA, USA, in 2015 and 2016, respectively. He is currently an Associate Professor at the Department of Land Surveying and Geo-Informatics, The Hong Kong Polytechnic University, Hong Kong, China. His research interests include remote sensing image processing, data fusion, vegetation remote sensing, nighttime light remote sensing, and urban remote sensing.

Jin Chen received the B.S. and M.S. degrees in geography from Beijing Normal University, Beijing, China, in 1989 and 1992, respectively, and the Ph.D. degree in civil engineering from Kyushu University, Fukuoka, Japan, in 2000.

From 2000 to 2001, he was a Post-Doctoral Fellow with the University of California at Berkeley, Berkeley, CA, USA, and from 2001 to 2004, he was with the National Institute for Environmental Studies, Tsukuba, Japan. He is currently a Professor with the State Key Laboratory of Earth Surface Processes and Resource Ecology, Beijing Normal University. His research interests include remote sensing modeling and vegetation parameter retrieval of remote sensing.